*International Journal of Minerals, Metallurgy and Materials*
*Volume 30, Number 1, January 2023, Page 144*
**https://doi.org/10.1007/s12613-022-2551-z**

# Tribological performance under different environments of Ti–C–N composite films for marine wear-resistant parts

*Hongbo Ju*[1,2),✉], *Rui Zhou*[1)], *Jing Luan*[1)], *Ch Sateesh Kumar*[3)], *Lihua Yu*[1)], *Junhua Xu*[1),✉], *Junfeng Yang*[5),✉], *Bowei Zhang*[6)], *and Filipe Fernandes*[2,4)]

1) School of Materials Science and Engineering, Jiangsu University of Science and Technology, Zhenjiang 212003, China
2) CEMMPRE—Centre for Mechanical Engineering Materials and Processes, Department of Mechanical Engineering, University of Coimbra, Coimbra 3030-788, Portugal
3) CFAA, University of the Basque Country UPV/EHU, Bilbao 48170, Spain
4) ISEP-School of Engineering, Polytechnic of Porto, Porto 4200-072, Portugal
5) Key Laboratory of Materials Physic, Institute of Solid State Physics, Hefei Institute of Physical Sciences, Chinese Academy of Sciences, Hefei 230031, China
6) Institute for Advanced Materials and Technology, University of Science and Technology Beijing, Beijing 100083, China
(Received: 26 July 2022; revised: 3 September 2022; accepted: 14 September 2022)

**Abstract:** The need for reducing the wear in mechanical parts used in the industry makes self-lubricant films one of the sustainable solutions to achieve long-term protection under different environmental conditions. The purpose of this work is to study the influence of C additions on the tribological behavior of a magnetron-sputtered TiN film in air, water, and seawater. The results show that the addition of C into the TiN binary film induced a new amorphous phase, and the films exhibited a dual phase of fcc (face-centered cubic)-TiN and amorphous carbon. The anti-friction and wear-resistance properties were enhanced in air and water by adding 19.1at% C. However, a further increase in the C concentration improved anti-frictional properties but also led to higher wear rates. Although the amorphous phase induced microbatteries and accelerated the corrosion of TiN phases in seawater, the negative abrasion state was detected for all Ti–C–N films due to the adhesion of the tribocorrosion debris on the wear track.

**Keywords:** RF reactive magnetron sputtering; Ti–C–N films; microstructure; tribological properties in air/water/seawater

## 1. Introduction

The sea has become an emerging field of human development due to its tremendous resources, thereby generating a steady increase in the demand for marine equipment for performing deep-sea oil/gas exploitations, finding alternative offshore green energy sources, and exploring marine fishing [1–5]. Steels are widely used in the marine equipment industry as structure materials for making mechanical components due to their excellent strength and toughness. However, complex ocean conditions could easily induce multifactor coupling damage to the tribological components of marine equipment by severe wear/corrosion/tribocorrosion. This condition leads to the irreversible degradation of equipment parts, resulting in huge losses [6–9]. In this regard, coating technology is one of the effective techniques for enhancing the surface performance of marine tribological components by either inducing self-lubrication and avoiding traditional liquid lubricants or improving the wear resistance for prolonged durability [10–13].

CrN and TiN nitride films synthesized using the physical vapor deposition method exhibited excellent wear resistance in seawater [14–16]. However, their columnar morphology could reduce the corrosion resistance as grain boundaries are open channels from where corrosive media can act [17]. Alloying metallic (Al and Mo) or nonmetallic (Si and B) elements into binary nitride films is one of the solutions to enhance the mechanical and seawater tribological performance of different films [18–21]. For instance, Cr–Si–N films exhibited better seawater tribological properties than CrN films due to the hydration tribocorrosion reaction between the amorphous phase of silicon nitride in the Cr–Si–N films and the seawater [22–23]. Zhang *et al.* [24] deposited a series of Cr–Ti–Si–C–N films onto 316L and TC4 substrates and investigated the tribological behavior of the coated samples in seawater. The results confirmed that the crystalline/amorphous microstructure helped in improving the wear and corrosion resistance in the seawater. Moreover, the carbon element could enhance self-lubrication and corrosion resistance, leading to improved tribological performances of the deposited films [25–29]. For example, Cheng *et al.* [30] synthesized a series of Ti–C–N films and found that the amorphous

✉ Corresponding authors: Hongbo Ju E-mail: hbju@just.edu.cn; Junhua Xu E-mail: jhxu@just.edu.cn; Junfeng Yang E-mail: jfyang@issp.ac.cn

phase of C with easy shear planes acted as a solid lubricant and contributed to the low friction coefficient (Cof.). Similar results were also reported in Ref. [31]. Moreover, carbon generally avoids the formation of columnar morphologies due to the formation of a nanocomposite structure (amorphous C + nitride/carbide grains) [32–34], thereby allowing enhance the hardness and toughness of films [35]. Although the mechanical components of marine systems operate under complex environmental conditions such as air, water, and seawater, the literature does not provide enough investigations that focus on the tribological behavior of films under different environmental conditions. Thus, in this study, the influence of carbon (C) addition on the tribological performance of Ti–C–N films under different environments (air, water, and seawater) was investigated.

## 2. Experimental

### 2.1. Deposition of films

Radiofrequency (RF) reactive magnetron sputtering system was used to deposit a series of Ti–C–N composite films with different carbon concentrations. The depositions were made using high-purity (99.9%) titanium and carbon targets with a 75 mm diameter. The three-dimensional schematic representation of the deposition system is shown in Fig. 1. Polished AISI 304 stainless steel (SS) and silicon (100) wafers were used as substrates. The substrates were first cleaned ultrasonically using alcohol for 15 min and acetone for 15 min and then dried using hot air before the deposition. The films deposited over the SS substrates were used to measure their mechanical and tribological properties, whereas silicon wafer substrates were used for electron probe microanalysis (EPMA), X-ray diffraction (XRD), X-ray photoelectron spectroscopy (XPS), and transmission electron microscopy (TEM) analyses. In particular, an interlayer of pure Ti was deposited on the substrates under the pure Ar atmosphere with a fixed Ti target power of 150 W for 15 min before the synthesis of the Ti–C–N composite film to improve their adhesion to the substrate. The detailed deposition parameters are summarized as follows: (i) background pressure was below $6.0 \times 10^{-4}$ Pa, and the deposition pressure was 0.3 Pa; (ii) the Ti target power was fixed at 200 W, whereas the C target power was varied between 0 and 120 W with an interval of 30 W; (iii) the argon-to-nitrogen flow ratio was 50/1.6 during the deposition; (iv) no substrate heating and bias voltage were applied; and (v) the deposition time was 3 h.

### 2.2. Film characterization

An electron probe microanalyzer (CAMECA SX-50, France) was used to analyze the elemental composition of the films. The crystal structure of the films was analyzed using an X-ray diffractometer (Shimazu-6000, Japan) with Cu $K_\alpha$ irradiation at 40 kV and 35 mA, and $2\theta$ was in the range of 30°–80° with a step of 2°/min. An X-ray photoelectron spectroscope (ESCALAB250XI, USA) was used to analyze the chemical bonding of the films, and Ag (3d 5/2, 368.2 eV) was used as the standard sample to calibrate the spectra. The film microstructure was also investigated using a transmission electron microscope (JEOL-2100F, Japan) with an accelerating voltage of 200 kV. The curvature radius was measured using the surface profiler (Bruker, Dektak-XT, Germany), and the residual stress of the films was calculated based on Stoney's equation [36]. A nano-indenter system (CPX + NHT2 + MST, Swiss) using a constant load of 3 mN for 10 s with an indentation depth of below 10% thickness of the films was applied to analyze the films' mechanical characteristics (hardness and elastic modulus). Nine points (3 × 3) at two different regions were chosen to evaluate the hardness and elastic modulus. The tribological behaviors in the air/water/seawater conditions were evaluated using the ball-on-disk wear tribometer (UMT-2, USA) with a counterpart of an alumina ball in a diameter of 9.4 mm. The test was run for 10 min. The sliding length was 10 mm, the applied load was 3 N, and the sliding speed was 60 mm/s. The relative humidity during all the tests was ~30%. The seawater was prepared according to the ASTMD 1141 98 standards. The experiment was repeated thrice to ensure the reproducibility of results. The coefficient of friction of the films was continuously recorded during the experiments. The wear rate (WR) was calculated using the Archard law. A scanning electron microscope and a Raman spectrometer (inVia, Renishaw, UK) were used to measure the wear track surface and tribo-phase on the wear track, respectively. The scanning vibrating electrode technique (SVET, VersaSCAN, Princeton Applied Research, USA) was applied to investigate the local corrosion behaviors of the films in the seawater as a function of testing times. A Pt–Ir micro electrode with a diameter of 10 μm was used as the scanning probe, with an amplitude of 30 μm and a frequency of 80 Hz.

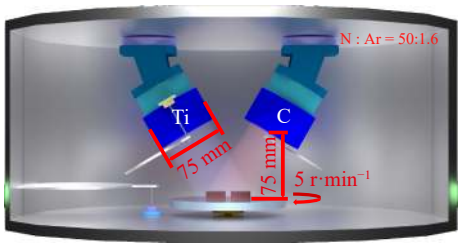


**Fig. 1. 3D schematic representation of the deposition system.**

## 3. Results and discussion

### 3.1. Elemental composition, structure, and microstructure

Table 1 illustrates the elemental chemical composition of the Ti–C–N films as a function of the power applied to the C target. All the films displayed an over stoichiometric composition, with the nitrogen concentration always above 50at%. The C concentration in the films gradually increased with the increase in the C target power, with a corresponding decrease in the Ti and N concentrations. The O concentration remained unchanged with the increasing power applied to the C target with a value of ~4at%.

Fig. 2 illustrates the XRD diffraction patterns of the reference TiN and Ti–C–N films with different C concentrations.

**Table 1. Elemental composition and residual stress of the Ti–C–N films as a function of the power of the C target**

| Power of C target / W | Elemental composition / at% | | | | Residual stress / GPa |
|---|---|---|---|---|---|
| | Ti | C | N | O | |
| 0 | 30.9 ± 2.0 | 0 | 55.5 ± 2.8 | 3.6 ± 0.2 | −0.78 ± 0.1 |
| 30 | 30.4 ± 1.5 | 12.1 ± 0.6 | 53.0 ± 2.7 | 4.5 ± 0.2 | −1.21 ± 0.1 |
| 60 | 27.8 ± 1.3 | 15.8 ± 0.8 | 52.3 ± 2.7 | 4.1 ± 0.2 | −1.31 ± 0.1 |
| 90 | 25.3 ± 1.3 | 19.1 ± 0.9 | 51.7 ± 2.6 | 3.9 ± 0.2 | −1.59 ± 0.1 |
| 120 | 20.4 ± 1.0 | 26.9 ± 1.3 | 47.9 ± 2.5 | 4.8 ± 0.2 | −1.39 ± 0.1 |

The XRD diffraction pattern of the TiN film displays two diffraction peaks positioned at ~37° and ~78° corresponding to a face-centered cubic (fcc) TiN phase (JCPDF card #65-0715). The addition of C into the TiN film decreases the intensity of the diffraction peaks. According to the literature, generally, when C is added to TiN films, it is incorporated in a solid solution in the TiN cell up to the saturation threshold (4.2at%) [37]. This condition justifies the shift of the diffraction peaks to higher angles with C incorporation. Moreover, the diffraction peak shifting is induced by the residual stress. Above the saturation value, the amorphous C phase surrounding the TiN grains is formed. Thus, less-intense diffraction peaks are detected as the amorphous phase inhibits the TiN grain growth. No diffraction peaks of the carbon phase can be detected due to its amorphous character [38].

The Raman spectra of the reference TiN and Ti–C–N films with different C concentrations are shown in Fig. 3. The spectrum of the reference TiN film does not exhibit any peak at the Raman vibration energy range of 1000–2210 $cm^{-1}$. However, when C is added to the film, two peaks at ~1580 and ~1834 $cm^{-1}$ can be observed, and the intensity increases with the increase in the C concentration. The peaks correspond to the D-peak (disorder peak, attributed to the breathing mode of $sp^2$ atoms) [39] and the G peak (carbon peak, attributed to the breathing of pairs of $sp^3$ atoms) [40] of the carbon phase.

The XPS spectrum of the film with a C concentration of 12.1at%, representative of all the C-doped coatings, is shown in Fig. 4. The black continuous line represents the original XPS peak, the color lines represent the peaks adjusted to the original XPS peak, and the interrupted black line represents the resultant of the fitting. Fig. 4(a) shows the total scanning spectrum of the sample. Five elements, i.e., Ti, Ag, C, N, and O, are observed. The signal of silver was not detected by the EPMA results from the reference Ag 3d to calibrate the binding energy. Fig. 4(b) shows that the Ti 2p spectrum fits eight peaks. Ti–N, Ti–O–N, Ti–N satellite, Ti–O, Ti–N, Ti–O–N, Ti–N satellite, and Ti–O bonds were detected in the Ti 2p XPS spectrum with energies of ~454.5, ~455.1, ~456.7, ~458.1, ~460.2, ~461.3, ~462.2, and ~463.2 eV, respectively [41]. The C 1s spectrum (Fig. 4(c)) is composed of three peaks at 284.8, 285.9, and 287.7 eV. The first two peaks correspond to the C–C bonds, whereas the last one refers to the C–N bonds [42]. The solid solution of C into the TiN lattice induces the appearance of C–N bonds, and the amorphous C phase surrounding the TiN grains may also establish C–N bonds with the neighborhood. The N 1s spectrum shown in Fig. 4(d) illustrates three peaks at ~396.3, ~396.9, and ~398.8 eV, corresponding to the N–(Ti,C), Ti–N, and C–N bonds, respectively [40,43]. Fig. 4(e) also exhibits three peaks at ~529.6, ~530.7, and ~532.9 eV, referring to the Ti–O, Ti–O–N, and C–O bonds, respectively [44].

The TEM analysis was performed to investigate the film microstructure, and the results of the film at 12.1at% C are shown in Fig. 5. The cross-sectional TEM image shown in Fig. 5(a) exhibits a dense morphology with no obvious columnar grains. Nevertheless, a dense columnar structure was detected in the TiN reference film based on our previous observations [44–47]. The selected-area electron diffraction (SEAD) pattern inset in Fig. 5(a) illustrates a series of diffraction rings corresponding to the fcc-TiN phase. Furthermore, the high-resolution transmission electron microscopy

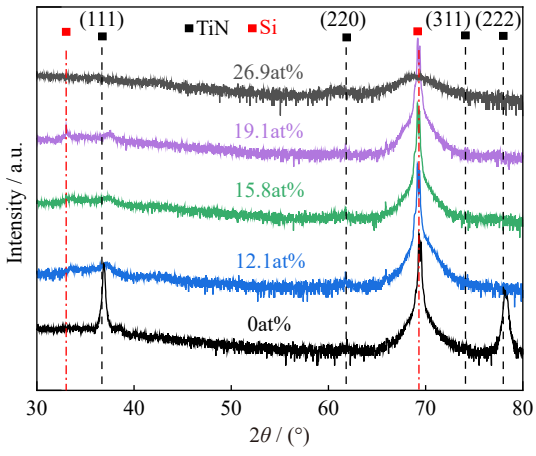


**Fig. 2. XRD diffraction patterns of the TiN and Ti–C–N films.**

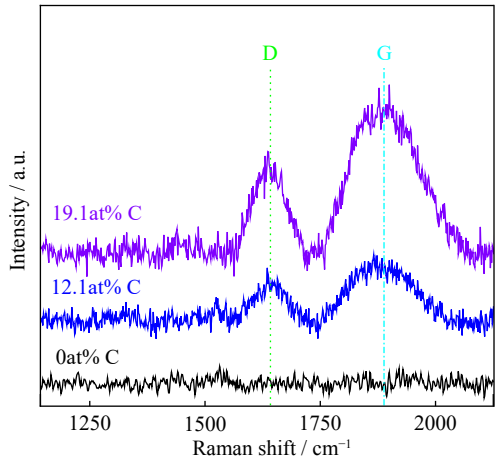


**Fig. 3. Raman spectra of the reference TiN film and Ti–C–N film with 12.1at% and 19.1at% of C.**

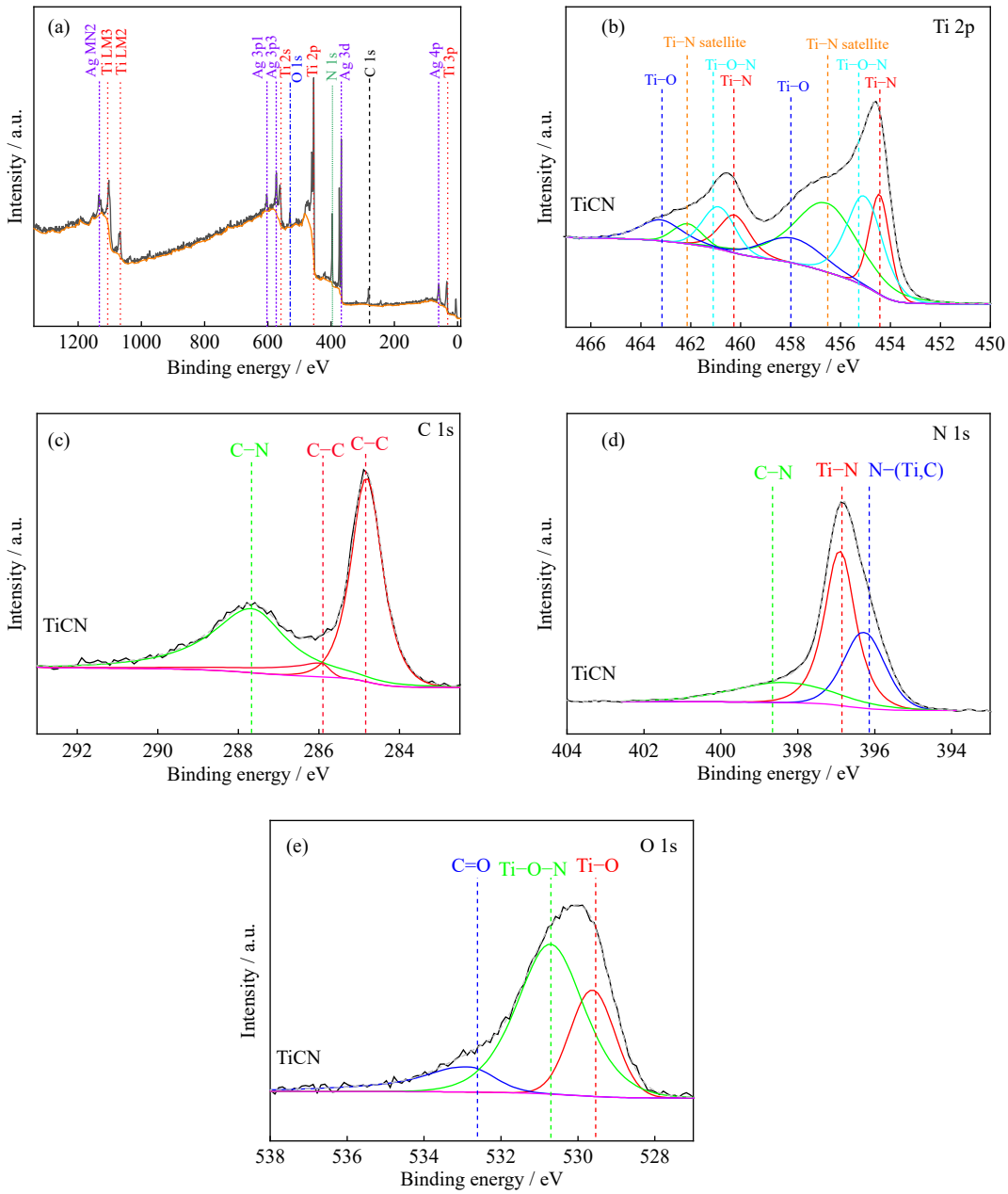


**Fig. 4. XPS spectra of the Ti–C–N film with 12.1at% of C: (a) survey scans, (b) Ti 2p, (c) C 1s, (d) N 1s, and (e) O 1s.**

(HRTEM) image of the film (Fig. 5(b)) illustrates the presence of crystalline and amorphous phases. The crystalline phase refers to the fcc-TiN that can be verified from its fast Fourier transform (FFT) and the inverse FFT (IFFT) patterns. Thus, a good agreement between the SEAD and XRD results shown previously was observed. The amorphous areas in this image correspond to the C phase.

The above results evidently show that the Ti–C–N films, regardless of the C concentration, consist of two phases, namely, crystalline fcc-TiN and amorphous C. Moreover, the films with C additions displayed a compact morphology.

### 3.2. Mechanical properties

The residual stresses at the reference TiN and Ti–C–N films with different C concentrations are listed in Table 1. All the films are in a compressive residual stress state. The increase in the C concentration on the reference film accounts for an increase in the residual stresses. The only exception is for the film with the highest C concentration of 25.6at%. Several factors can contribute to the increase in residual stresses. First, it may be due to the lattice distortion induced by the solid solution of C into the TiN lattice, which could increase the compressive residual stress of the films. Second, it can be due to the different thermal expansion coefficients between the film and substrate. The thermal stress of the films could be calculated based on the equation form, and its value is mainly attributed to the thermal expansion coefficient and deposition temperature [48]. Nevertheless, the deposition temperature exhibits little dependence on the C concentration, and its value remained in the range of 80–100°C during the deposition. The thermal expansion coefficients of TiN and C are $6.0 \times 10^{-6}$ [49] and $1.2 \times 10^{-6}$ °C$^{-1}$ [50], respectively. Thus, the thermal residual stress of all the films is tensile regardless of the C concentration, and the formation of

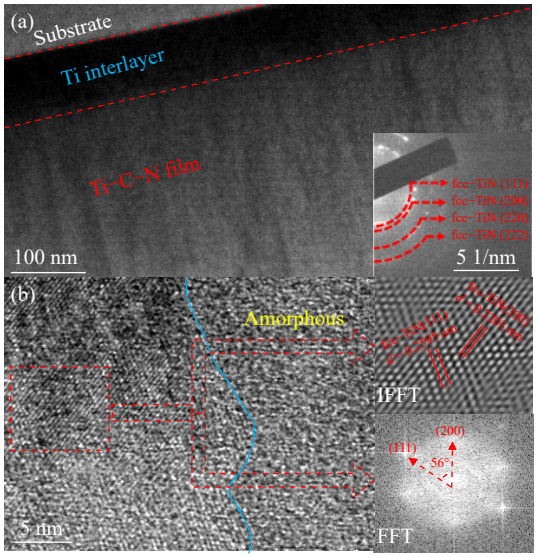


**Fig. 5. (a) Cross-sectional TEM image and its corresponding SEAD pattern and (b)HRTEM image and the FFT and IFFT patterns from the crystalline area of the film with 12.1at% of C.**

the amorphous phase of carbon could drop the thermal expansion coefficient value of the composite films. Based on the above mentioned three factors, the increase in the residual stress of films is mainly attributed to the lattice distortion and differences in the thermal expansion coefficient between the film and substrate. However, the formation of a large amount of amorphous phase decreases the residual stress for the film with a high C concentration.

Fig. 6 shows the hardness ($H$) and elastic modulus ($E$) of the TiN and Ti–C–N films with different C concentrations. A gradual increase in the hardness and elastic modulus took place with the increase in the C concentration up to ~15at% C. However, at ~19at% C, a sudden spike in both properties was recorded. A further increase in the C concentration resulted in a significant drop in both the measured properties.

The enhancement of hardness can be attributed to three main factors: (i) solid solution hardening induced by the substitution of C into the TiN lattice attributes to the enhancement of the hardness, (ii) increase in the residual compressive stress on the films [51], and (iii) the amorphous phase inhibiting the growth of Ti–C–N grains (broad diffraction peaks are seen in Fig. 2 when C is added) [52]. The drop in the film hardness with the highest C is attributed to the formation of a large amount of soft and amorphous C phase in the films. The decrease in the residual stress on the film can also account for this effect.

The plastic deformation resistance factor, i.e., the $H^3/E^2$ ratio, is another important mechanical parameter to consider as it indicates film toughness [53]. The values as functions of the C concentration are displayed in Fig. 6. The $H^3/E^2$ ratio of the reference TiN film was ~0.1 GPa. In general, when C is added to the reference film, their fracture toughness is improved. The film interfaces could be increased by the formation of the amorphous phase of C, thereby inducing microcrack deflection to enhance toughness [53]. However, C concentrations higher than ~19at% result in a slight drop in the

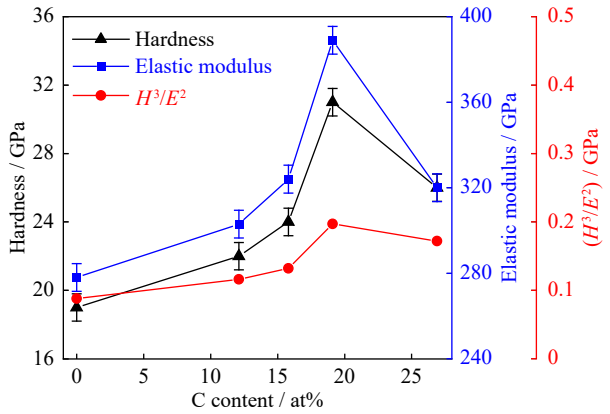


**Fig. 6. Hardness, elastic modulus, and $H^3/E^2$ ratio of the reference TiN and Ti–C–N films with different C concentrations.**

$H^3/E^2$ ratio to ~0.18 GPa due to the high amounts of the amorphous phase of C.

### 3.3. Tribological properties

Fig. 7 illustrates the friction curves of the Ti–C–N films with different C concentrations in air, water, and seawater. All curves, regardless of the C concentrations, could be divided into two stages: the running-in stage and the stable stage. The addition of C into the TiN reference could significantly drop the Cof.

Fig. 8 shows the Cof. and WR of the Ti–C–N films with different C concentrations in air, water, and seawater. The addition of C concentration to the TiN film reduced the Cof. of the films under all the environments. For the tests conducted in air and water (Fig. 8(a) and (b)), the specific WR also progressively decreases with C concentration up to 19.1at% of C. Nonetheless, with the higher C concentration, the Cof. decreased and the WR increased for the film. This result is attributed to the loss of the mechanical properties of the film with a high C concentration, as presented in the previous subsection. For tests conducted in seawater (Fig. 8(c)), the only film displaying wear is the reference TiN film. All the C-rich films did not display any wear, and only wear debris adhered to the wear track surface was observed.

Fig. 9 shows the wear track surface image and corresponding 2D profiles of the wear track under different testing conditions. Scratches parallel to the sliding movement of the ball appeared on the wear track of the film with 12.1at% C tested in air (Fig. 9(a)). During the tests, asperities of the film surface in contact with the counterpart broke under the shear force, forming the initial wear debris. Due to the ball movements, the particles were dragged to the surface, creating scratches. Increasing the C concentration to 19.1at% slowed down the interaction between the counterparts, leading to a very smooth wear track surface, as detected in Fig. 9(b). The wear track of the film in the water at 12.1at% C exhibited grooves and furrows, as shown in Fig. 9(c). The width of the wear track is ~500 μm with a depth below 0.5 μm. The asperities from the film and counterpart surface could be easily crushed under the load force and then moved with the counterpart under the shear force. Micropores might be formed by

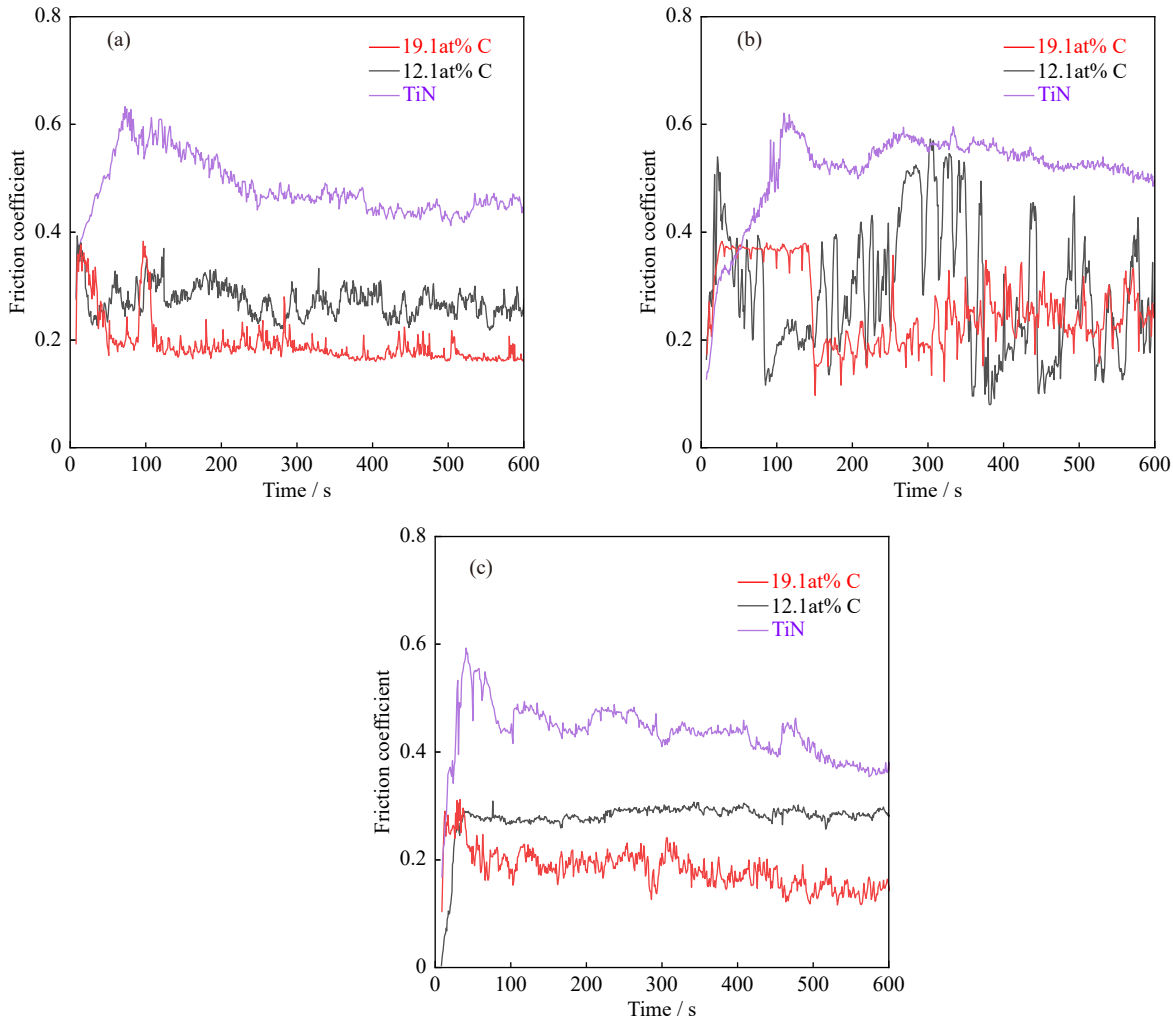


**Fig. 7. Friction curves vs. testing time of the Ti–C–N films with different C concentrations in (a) air, (b) water, and (c) seawater.**

the brittle phase fracture of TiN. The hard debris could scratch the wear track surface and thereby induce the formation of grooves and furrows. Increasing the C concentration to 19.1at% enhanced the wear-resistance performance by causing a reduction in the width and depth of the wear track to ~400 and ~0.25 μm, respectively (Fig. 9(d)). The disappearance of grooves and furrows also confirms the self-lubricant properties of the amorphous phase of C in the films. As far as the wear test in seawater is considered, obvious debris induced by the tribocorrosion reactions was detected on the wear track surface (Fig. 9(e) and (f)). The value of the WR is negative due to the significant amount of adhered tribocorrosion products in the wear track.

The Raman spectra from the wear track surface of the film for different environment conditions at 12.1at% C are shown in Fig. 10. The purpose of this investigation was to study the formation of the tribo phase on the wear track in different testing environments. Moreover, the spectrum of the as-deposited film is plotted for reference purposes. Two peaks at ~217 and ~311 $cm^{-1}$ with a low density appeared in the spectrum of the as-deposited film, and both peaks refer to the TiN phase [54]. Moreover, the other two peaks at ~1571 and ~1835 $cm^{-1}$ corresponding to the G ($sp^2$) [38] and D ($sp^3$) [39] peaks, respectively, were detected. The spectrum from the wear track surface in the air still exhibited four peaks, which are similar to that from the as-deposited film. No other peak corresponding to $TiO_2$ was detected. However, the spectrum from the wear track surface in the water exhibited the other peaks at ~400 and ~640 $cm^{-1}$ corresponding to $TiO_2$ [55]. Tribo-chemical is induced by the interaction between the counterpart and film in the water and is finally attributed to the formation of the tribo phase of $TiO_2$. Many peaks assigned to the $TiO_2$ peaks appeared in the spectrum of the wear track in the seawater. Tribocorrosion activities are thus attributed to the formation of the $TiO_2$ phase in the seawater.

The SVET system was applied to investigate the potential tendency as a function of the testing time in seawater, and the corresponding potential map is shown in Fig. 11. As shown in Fig. 11(a), uneven corrosion activities could be detected for the TiN film surface at 0 h, and all values of the current densities in the map exhibit a positive state. The grain boundaries of the TiN film usually induce priority corrosion and attribute to the high value of the current density (red area in the map). The positively dense thin film ($TiO_2$) could be easily formed by the chemical corrosion action between the NaCl solution and TiN film [56], and it could play the anticorrosion role by preventing the permeation of the NaCl solution into the inner part of the films [57]. Therefore, an enhanced

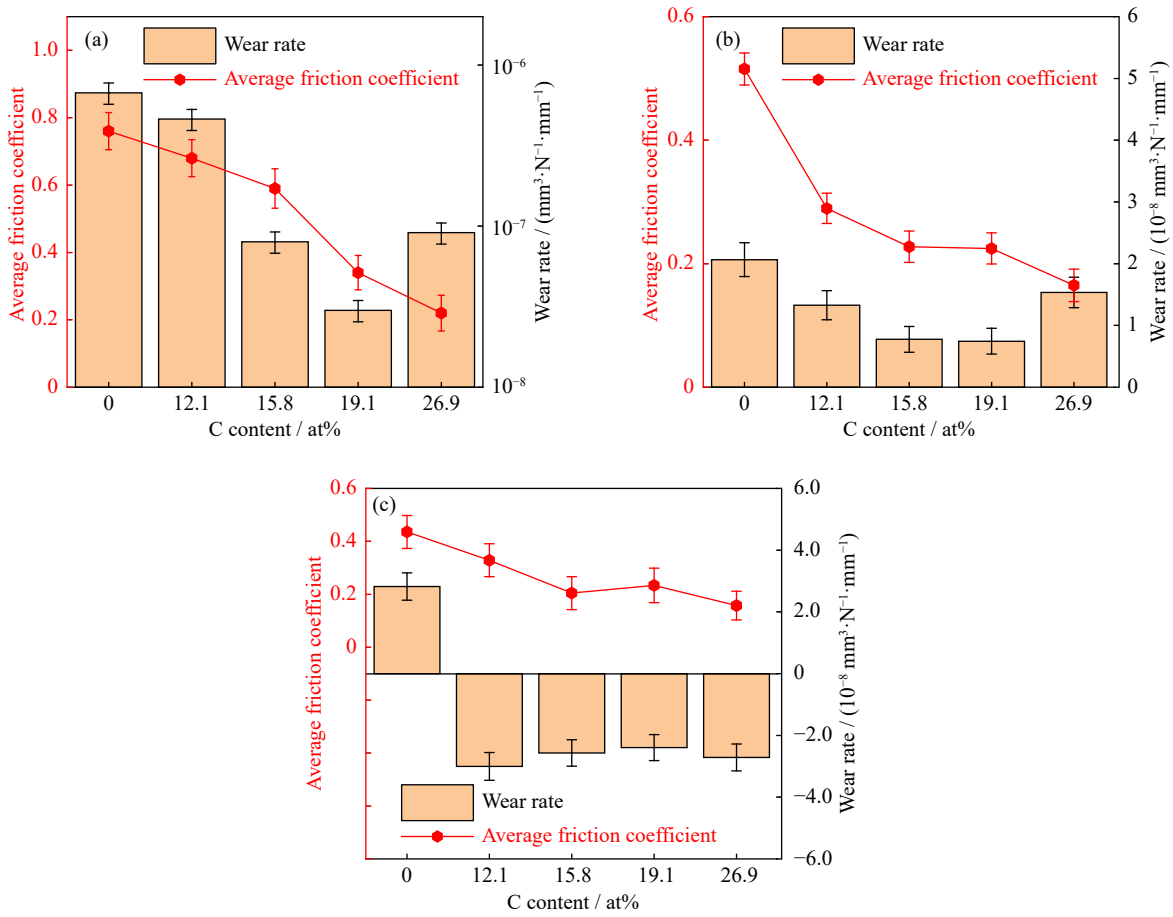


**Fig. 8. Friction coefficient and wear rates of the Ti–C–N films with different C concentrations under different testing environments: (a) air, (b) water, and (c) seawater.**

anticorrosion performance could be detected at 1 h, as shown in Fig. 11(b), and the area marked in red with a high current density sharply dropped. However, uneven corrosion activities still existed during this period. This condition might also be attributed to grain boundaries, which easily induce intergranular corrosion. The addition of C into the TiN film changes their corrosion behavior. Although the SVET map in Fig. 11(c) was utilized when the sample was immersed in the seawater at 0 h, the time of scanning of the Pt probe from the top to the bottom of the figure could be 0.5 h. The results in Fig. 11(c) confirm a significant corrosion susceptibility as a function of the testing time. Moreover, uniform corrosion could be considered the main corrosion behavior for the Ti–C–N film at 12.1at% C, and the uniform distribution of the amorphous phase of carbon into the TiN matrix could induce a form of local microbatteries between the amorphous and TiN nanocrystalline phases. This result is attributed to the acceleration of the TiN phase. Accordingly, the current density in Fig. 11(c) is higher than that in Fig. 11(a). A further increase of the testing time to 1 h leads to uniform corrosion with a high current density of ~50–60 μA·cm$^{-2}$. The corrosion of the film is aggravated by local microbatteries with an increase in the testing time.

The passive protection oxide-based thin film could be easily formed on the film surface in the seawater, which was also reported for nitride-based films [58]. However, it could be easily worn out to expose the fresh as-deposited TiN phase by the counterpart during the wear test, which causes further penetration of the seawater into the inner part of the films through the channel of the grain boundaries of TiN. Therefore, tribocorrosion could be aggravated by the movements of the counterpart, inducing a significant production of the $TiO_2$ phase on the wear track. The tribocorrosion production results in scratches in the wear track surface and degrades the wear-resistance performance of the TiN film. This outcome justifies the highest WR value in seawater. The addition of C to the TiN film results in the disappearance of the columnar grain structure and induces the formation of the microstructure of TiN crystals embedded into the amorphous phase of carbon. The disappearance of the penetration channels of grain boundaries could prevent the tribocorrosion reaction. However, local microbatteries are also formed between the amorphous and TiN phases due to the different anticorrosion performances, and this condition accelerated the tribocorrosion of TiN phases on the film surface. The tribocorrosion mechanism diagram of the Ti–C–N films is shown in Fig. 12. The relative concentration of TiN decreases with the increase in the concentration of the amorphous phases, and it finally reduces the concentration of the TiN phase involved in the tribocorrosion reaction. The high hardness of the Ti–C–N films also enhances the load-bearing capacity. The previous factors contribute to the enhancement of the wear

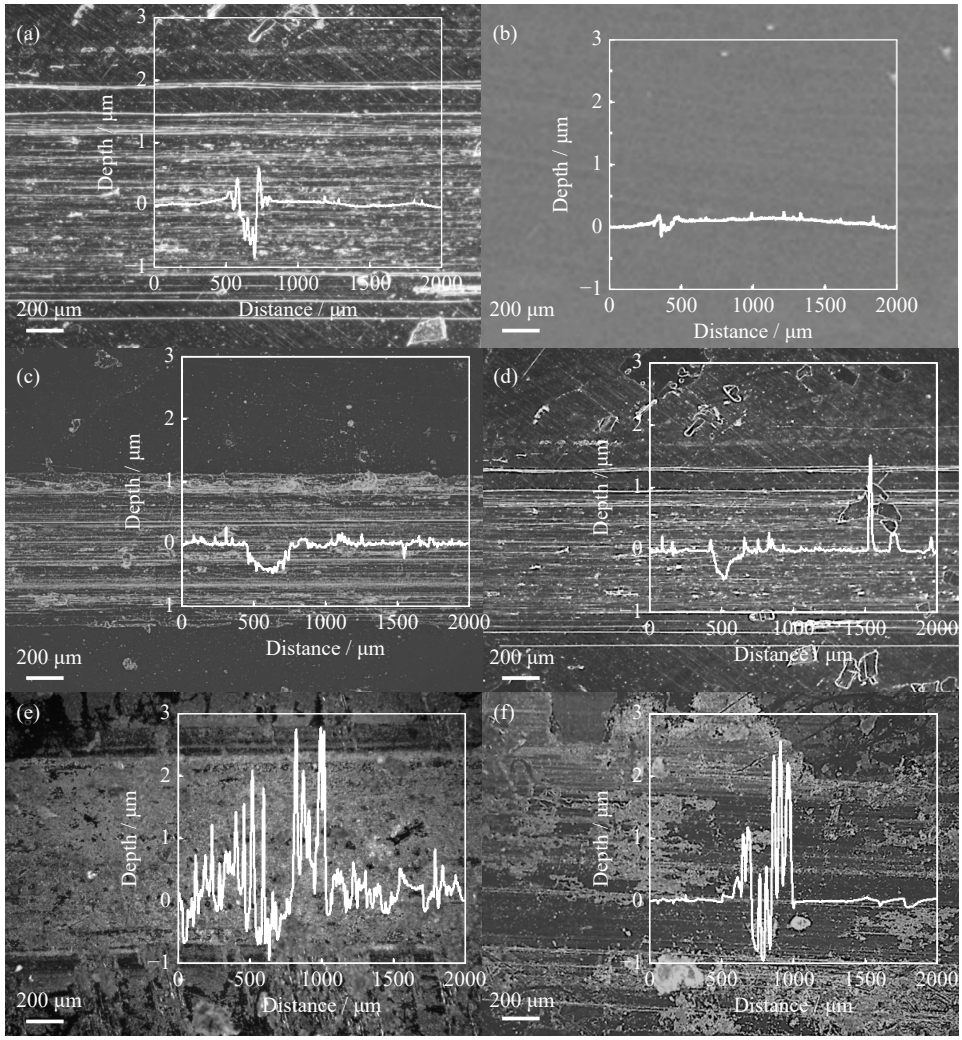


**Fig. 9. Wear track surface images in the air for the film at (a) 12.1at% and (b) 19.1at% C, in the water for the film at (c) 12.1at% and (d) 19.1at% C, and in the seawater for the film at (e) 12.1at% and (f) 19.1at% C.**

resistance of the deposited films.

Based on the results, it can be concluded that increasing the C concentration in a TiN film improves its tribological performance. The C-rich transfer tribo layer was easily formed during the wear test under the counterpart to reduce the shear and stress effects, act as a solid lubricant, and enhance the antifriction performances [59–60]. The high intensity of the G peak from the wear track surface after the wear test in the air also confirms this conclusion (see Fig. 9). Moreover, the consequence of the repeated friction load and frictional heat could induce the regraphitization of the C phase in the composite films and finally form the lubricant thin film on the wear track to lubricate the films [61]. The main factors explaining the improvements in the WR are as follows:

(i) High hardness. High hardness ensures a high capacity of load bearing during the wear test, which could enhance the wear resistance in some sense.

(ii) Lubricant phases in the deposited films. A continuous provision of the lubricant phase softens the interaction between the counterpart and wear track surface and thereby reduces the WR during the wear testing.

(iii) Fracture toughness. The formation of amorphous

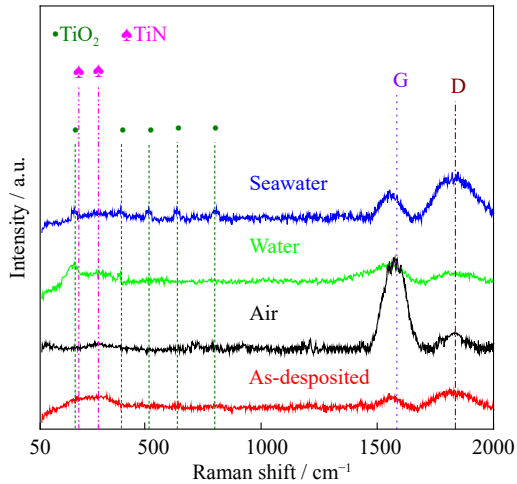


**Fig. 10. Raman spectra of the as-deposited films and the wear track surface after the wear test in air, water, and seawater.**

phases in the films could induce more interfaces, and this limits initial crack sizes and also helps deflect and terminate the crack growth.

Therefore, the addition of C enhances the fracture toughness and thereby improves the capacity to avoid cracks dur-

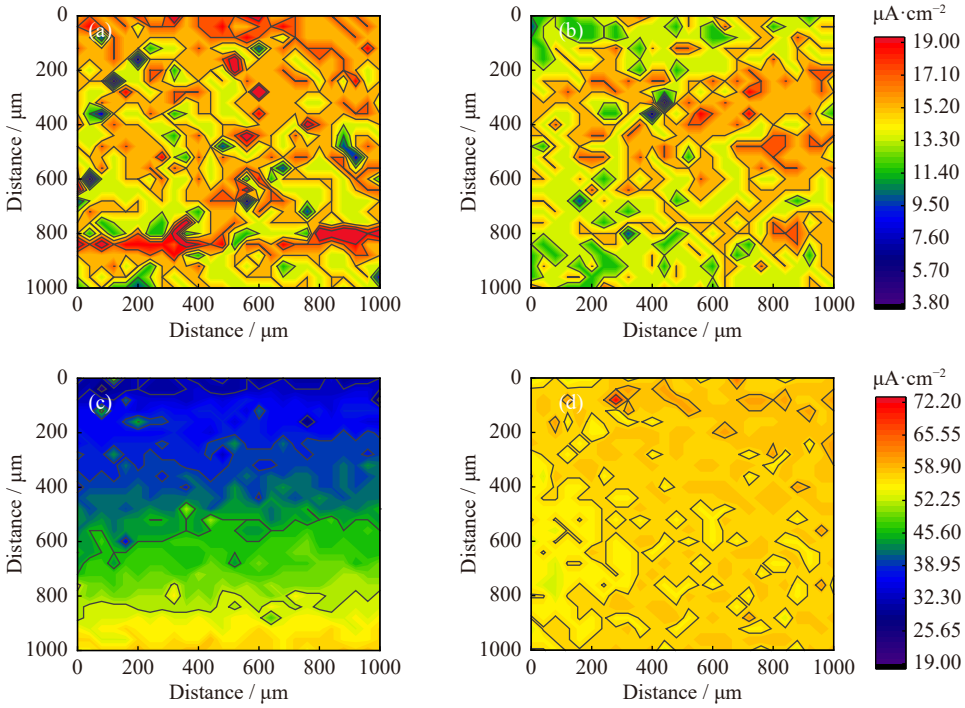


**Fig. 11. SVET potential maps of the TiN and Ti–C–N films in seawater as a function of the testing time: (a) 0 h and (b) 1 h for the TiN film, and (c) 0 h and (d) 1 h for the Ti–C–N film at 12.1at% C.**

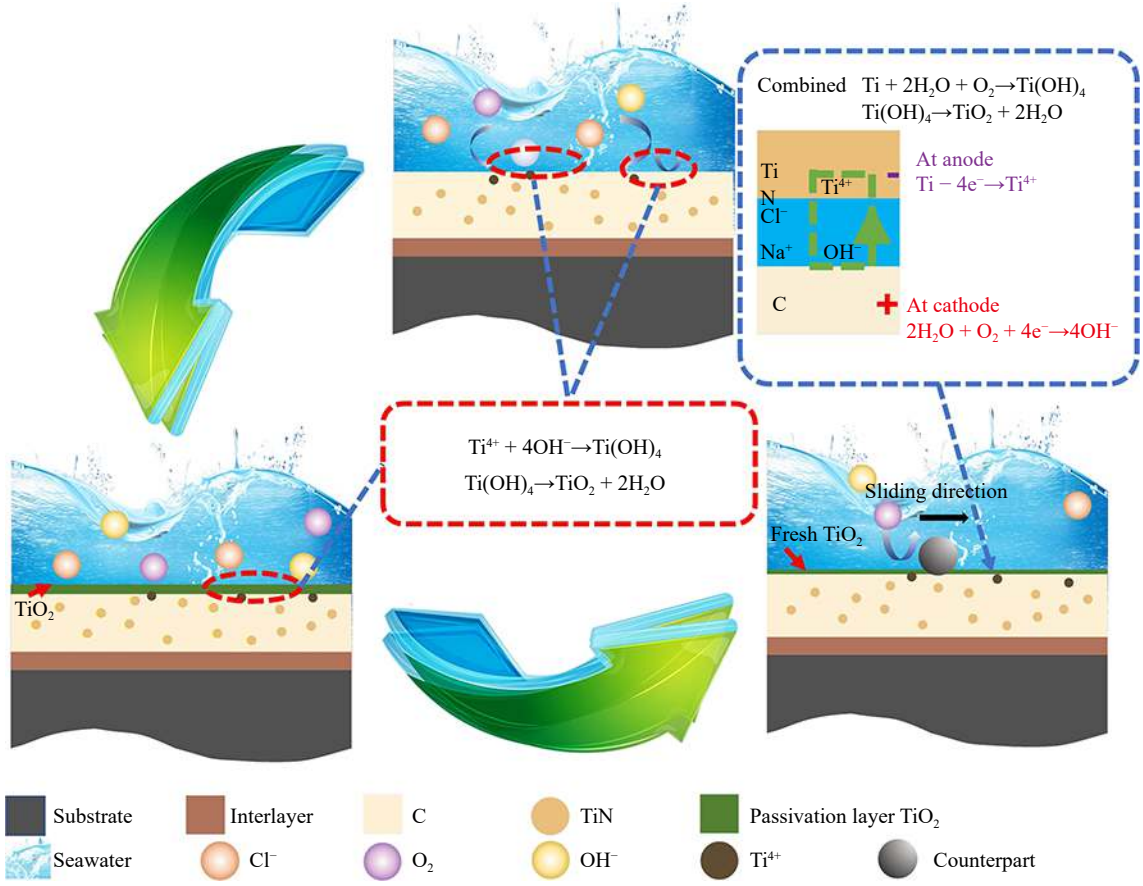


**Fig. 12. Tribocorrosion mechanism diagram of the Ti–C–N films.**

ing the wear test. The enhancement of the fracture toughness could also be demonstrated by the value of the $H^3/E^2$ ratio for the film with a C concentration of <19.1at%. However, the drop in the hardness and $H^3/E^2$ ratio reduced the WR value with a further increase in the C concentration from 19.1at% to 26.9 at%.

For the tribological results from water conditions, the wear mechanism is similar to that in the air. However, water could

play the lubricant role during the wear test, which thereby induces a low value of Cof. and WR of all films in water than that with the same C concentration in the air. In addition, an approximate C concentration makes Cof. decrease proportionally due to the formation of lubricant C in the TiN matrix.

For the tribological behaviors in the seawater, the tribocorrosion production of $TiO_2$ exhibited a relatively higher Cof. compared with a TiN film [62]. Therefore, the Cof. of the Ti–C–N films is higher than that in the water. Local microbatteries on the film surface could be induced by the seawater's high corrosion resistance of the amorphous phase of C to accelerate the formation of the tribocorrosion production of $TiO_2$ and finally attribute to a negative WR of the Ti–C–N film with high hardness. Moreover, some other factors, such as hardness, $H^3/E^2$ ratio, and compactness level, of the structure contribute to the enhancement of the films' wear resistance.

## 4. Conclusions

A series of Ti–C–N composite films were synthesized using the RF magnetron sputtering system to investigate the influence of carbon (C) addition on the tribological performance of the Ti–C–N films under different environments (air, water, and seawater). The major conclusions that can be drawn from the present investigation are as follows.

(1) The Ti–C–N films exhibited a dual phase of fcc-TiN and amorphous carbon, and the addition of C led to a compact morphology.

(2) The addition of C also enhanced the hardness of the Ti–C–N films to ~32 GPa at 19.1at% C. Solid solution strengthening, refinement of the grain of the TiN crystallites, and the increase of the compressive residual stress were the main reasons for this enhancement.

(3) The antifriction properties were enhanced in air and water by adding 19.1at% C due to the lubricant role from the C phase in the films. Moreover, the enhanced hardness and $H^3/E^2$ ratio enhanced the wear-resistance performance in the air and water. Although the amorphous phase induced microbatteries and thereby accelerated the corrosion of the TiN phases of the film surface in seawater, the negative abrasion state was detected for all the Ti–C–N films due to the adhesion of the tribocorrosion debris on the wear track.

## Acknowledgements

This work was financially supported by the National Natural Science Foundation of China (Nos. 52171071, 52172090, 52071159, and 51801081), Portugal National Funds through FCT project (No. 2021.04115), FEDER National funds FCT under the project CEMMPRE–UIDB/00285/2020, Outstanding University Young Teachers of "Qing Lan Project" of Jiangsu Province, Excellent Talents of "Shenlan Project" of Jiangsu University of Science and Technology, and China Merchants Marine Scientific Research and Innovation Fund. Filipe Fernandes acknowledges the funding received in the aim of the projects: MCTool[21]–ref. "POCI-01-0247-FEDER-045940", CEMMPRE–ref. "UIDB/00285/2020", and SMARTLUB–ref. "POCI-01-0145-FEDER-031807".

## Conflict of Interest

The authors declare no conflict of interest.

## References

[1] R. Grinon-Echaniz, P. Refait, M. Jeannin, *et al*., Study of cathodic reactions in defects of thermal spray aluminium coatings on steel in artificial seawater, *Corros. Sci.*, 187(2021), art. No. 109514.

[2] D.P. Wang, G. Chen, A.D. Wang, *et al.*, Corrosion behavior of single- and poly-crystalline dual-phase TiAl–$Ti_3Al$ alloy in NaCl solution, *Int. J. Miner. Metall. Mater.*, 2022. DOI: 10.1007/s12613-022-2513-5

[3] H.S. Wu, G.Z. Shen, R.X. Li, *et al*., Influence of embedded reduced graphene oxide on the corrosion-wear performance of cold sprayed Zn-rGO/Al coating in NaCl solution, *Surf. Coat. Technol.*, 429(2022), art. No. 127856.

[4] D. Saran, A. Kumar, S. Bathula, D. Klaumünzer, and K.K. Sahu, Review on the phosphate-based conversion coatings of magnesium and its alloys, *Int. J. Miner. Metall. Mater.*, 29(2022), No. 7, p. 1435.

[5] M.D. Zhang, F. Zhou, Y.J. Wu, Q.Z. Wang, and Z.F. Zhou, Microstructure and electrochemical characteristics of CrMoN/Ag nanocomposite coatings in seawater, *Surf. Coat. Technol.*, 441(2022), art. No. 128551.

[6] H.B. Ju, D. Yu, J.H. Xu, *et al*., Crystal structure and tribological properties of ZrAlMoN composite films deposited by magnetron sputtering, *Mater. Chem. Phys.*, 230(2019), p. 347.

[7] W. Liu, J.X. Li, H.Y. Xu, J. Li, and X.P. Qiu, Stabilized cobalt-free lithium-rich cathode materials with an artificial lithium fluoride coating, *Int. J. Miner. Metall. Mater.*, 29(2022), No. 5, p. 917.

[8] H.B. Ju, D. Yu, L.H. Yu, *et al*., The influence of Ag contents on the microstructure, mechanical and tribological properties of ZrN–Ag films, *Vacuum*, 148(2018), p. 54.

[9] H.B. Ju, D. Yu, J.H. Xu, *et al*., Microstructure, mechanical, and tribological properties of niobium vanadium carbon nitride films, *J. Vac. Sci. Technol. A*, 36(2018), No. 3, art. No. 031511.

[10] R. Wang, J.X. Deng, Z.H. Zhang, *et al*., Microstructure and wear performance of electro-sprayed self-lubricating $Ni_3Al/Cr_3C_2$–$MoS_2$ composite films, *Surf. Coat. Technol.*, 428(2021), art. No. 127862.

[11] H.B. Ju, N. Ding, J.H. Xu, *et al*., Improvement of tribological properties of niobium nitride films via copper addition, *Vacuum*, 158(2018), p. 1.

[12] Y.J. Tarzanagh, D. Seifzadeh, and R. Samadianfard, Combining the 8-hydroxyquinoline intercalated layered double hydroxide film and sol–gel coating for active corrosion protection of the magnesium alloy, *Int. J. Miner. Metall. Mater.*, 29(2022), No. 3, p. 536.

[13] R. Zhou, H.B. Ju, S.J. Liu, *et al*., The influences of Ag content on the friction and wear properties of TiCN–Ag films, *Vacuum*, 196(2022), art. No. 110719.

[14] Y. Xia, Z.G. Xu, J. Peng, Q. Shen, and C.B. Wang, *In-situ* formation, structural transformation and mechanical properties CrN coatings prepared by MPCVD, *Surf. Coat. Technol.*, 441(2022), art. No. 128522.

[15] R. Akhter, Z.F. Zhou, Z.H. Xie, and P. Munroe, TiN versus TiSiN coatings in indentation, scratch and wear setting, *Appl.*

*Surf. Sci.*, 563(2021), art. No. 150356.
[16] M. Jafari, L. Rogström, J.M. Andersson, *et al*., Thermal degradation of TiN and TiAlN coatings during rapid laser treatment, *Surf. Coat. Technol.*, 422(2021), art. No. 127517.
[17] H.B. Ju, R. Zhou, S.J. Liu, *et al*., Enhancement of the tribological behavior of self-lubricating nanocomposite $Mo_2N$/Cu films by adding the amorphous $SiN_x$, *Surf. Coat. Technol.*, 423(2021), art. No. 127565.
[18] H.B. Ju, N. Ding, J.H. Xu, *et al*., The tribological behavior of niobium nitride and silver composite films at elevated testing temperatures, *Mater. Chem. Phys.*, 237(2019), art. No. 121840.
[19] C.K. Liu, H.B. Ju, J.H. Xu, *et al*., Influence of copper on the compositions, microstructure and room and elevated temperature tribological properties of the molybdenum nitride film, *Surf. Coat. Technol.*, 395(2020), art. No. 125811.
[20] H.B. Ju, R. Wang, W.X. Wang, *et al*., The microstructure and tribological properties of molybdenum and silicon nitride composite films, *Surf. Coat. Technol.*, 401(2020), art. No. 126238.
[21] H.B. Ju, N. Ding, J.H. Xu, *et al*., The influence of crystal structure and the enhancement of mechanical and frictional properties of titanium nitride film by addition of ruthenium, *Appl. Surf. Sci.*, 489(2019), p. 247.
[22] S.Q. Song, X.F. Cui, G. Jin, *et al*., Effect of N + Cr ions implantation on corrosion and tribological properties in simulated seawater of carburized alloy steel, *Surf. Coat. Technol.*, 385(2020), art. No. 125357.
[23] Y.Q. Fu, F. Zhou, and M.D. Zhang, The enhancement of individual friction and corrosion properties of CrSiN coatings by Mo doping in seawater, *Surf. Coat. Technol.*, 432(2022), art. No. 128069.
[24] P. Zhang, L. Shan, X.L. Su, *et al*., Microstructure and tribological performance of CrTiSiCN coatings on 316L and TC4 in seawater, *Tribol. Int.*, 156(2021), art. No. 106832.
[25] J. Takadoum, H.H. Bennani, and M. Allouard, Friction and wear characteristics of TiN, TiCN and diamond-like carbon films, *Surf. Coat. Technol.*, 88(1997), No. 1-3, p. 232.
[26] C.K. Liu, H.B. Ju, P.X. Han, *et al*., The influence of carbon content on the microstructure, mechanical and frictional property of chromium carbon nitride composite films, *Vacuum*, 178(2020), art. No. 109368.
[27] X.R. Deng, H. Kousaka, T. Tokoroyama, and N. Umehara, Tribological behavior of tetrahedral amorphous carbon (ta-C) coatings at elevated temperatures, *Tribol. Int.*, 75(2014), p. 98.
[28] G.F. Zheng, Q. Jiao, C. Li, *et al*., Influence of nitridation on the microstructure and corrosion behavior of reactive plasma sprayed TiCN coatings, *Surf. Coat. Technol.*, 396(2020), art. No. 125954.
[29] H.B. Ju, R. Wang, N. Ding, *et al*., Improvement on the oxidation resistance and tribological properties of molybdenum disulfide film by doping nitrogen, *Mater. Des.*, 186(2020), art. No. 108300.
[30] Y.H. Cheng, T. Browne, B. Heckerman, and E.I. Meletis, Influence of the C content on the mechanical and tribological properties of the TiCN coatings deposited by LAFAD technique, *Surf. Coat. Technol.*, 205(2011), No. 16, p. 4024.
[31] B. Yi, S.H. Zhou, Z.G. Qiu, and D.C. Zeng, The influences of pulsed bias duty cycle on tribological properties of solid lubricating TiMoCN coatings, *Vacuum*, 180(2020), art. No. 109552.
[32] H.B. Ju, R. Zhou, J. Luan, *et al*., Multilayer $Mo_2N$–Ag/$SiN_x$ films for demanding applications: Morphology, structure and temperature-cucling tribological properties, *Mater. Des.*, 223(2022), art. No. 111128.
[33] J.G. Qian, S.X. Li, J.B. Pu, *et al*., Effect of heat treatment on structure and properties of molybdenum nitride and molybdenum carbonitride films prepared by magnetron sputtering, *Surf. Coat. Technol.*, 374(2019), p. 725.
[34] D. Özkan, M.A. Yılmaz, C. Erdem, *et al*., Wear and friction behavior of CrTiN/TiCN and CrTiN/CrCN multilayer composite coatings, *Ceram. Int.*, 48(2022), No. 10, p. 13732.
[35] H.Q. Wang, Y. Ou, X. Zhang, *et al*., Tribocorrosion behaviors of TiSiCN nanocomposite coatings deposited by high power impulse magnetron sputtering, *Mater. Res. Express*, 7(2020), art. No. 076407.
[36] O. Savchuk and A.A. Volinsky, Nonparametric estimation of SiC film residual stress from the wafer surface profile, *Measurement*, 177(2021), art. No. 109238.
[37] N. Madaoui, N. Saoula, B. Zaid, D. Saidi, and A.S. Ahmed, Structural, mechanical and electrochemical comparison of TiN and TiCN coatings on XC48 steel substrates in NaCl 3.5% water solution, *Appl. Surf. Sci.*, 312(2014), p. 134.
[38] P.B. Mi, J.N. He, Y.F. Qin, and K. Chen, Nanostructure reactive plasma sprayed TiCN coating, *Surf. Coat. Technol.*, 309(2017), p. 1.
[39] J.C. Sánchez-López, M.D. Abad, I. Carvalho, *et al*., Influence of silver content on the tribomechanical behavior on Ag–TiCN bioactive coatings, *Surf. Coat. Technol.*, 206(2012), No. 8-9, p. 2192.
[40] R. Chen, J.P. Tu, D.G. Liu, Y.J. Mai, and C.D. Gu, Microstructure, mechanical and tribological properties of TiCN nanocomposite films deposited by DC magnetron sputtering, *Surf. Coat. Technol.*, 205(2011), No. 21-22, p. 5228.
[41] X.X. Liu, N. Umehara, T. Tokoroyama, and M. Murashima, Tribological properties of ta-$CN_x$ coating sliding against steel and sapphire in unlubricated condition, *Tribol. Int.*, 131(2019), p. 102.
[42] Y.F. Qin, G.F. Zheng, L.Y. Zhu, *et al*., Structure and wear characteristics of TiCN nanocomposite coatings fabricated by reactive plasma spraying, *Surf. Coat. Technol.*, 342(2018), p. 137.
[43] F.Y. Yan, B.L. Jiang, Z.Y. Wang, *et al*., Thermal stabilization of nanocrystalline promoting conductive corrosion resistance of TiN–Ag films for metal bipolar plates, *Vacuum*, 195(2022), art. No. 110631.
[44] H. Cicek, Wear behaviors of TiN/TiCN/DLC composite coatings in different environments, *Ceram. Int.*, 44(2018), No. 5, p. 4853.
[45] H.B. Ju, L.H. Yu, S. He, *et al*., The enhancement of fracture toughness and tribological properties of the titanium nitride films by doping yttrium, *Surf. Coat. Technol.*, 321(2017), p. 57.
[46] H.B. Ju and J.H. Xu, Microstructure, oxidation resistance, mechanical and tribological properties of Ti–Y–N films by reactive magnetron sputtering, *Surf. Coat. Technol.*, 283(2015), p. 311.
[47] C.K. Liu, H. Ju, L.H. Yu, *et al*., Tribological properties of $Mo_2N$ films at elevated temperature, *Coatings*, 9(2019), No. 11, p. 734.
[48] A. Erdemir, A crystal chemical approach to the formulation of self-lubricating nanocomposite coatings, *Surf. Coat. Technol.*, 200(2005), No. 5-6, p. 1792.
[49] T.W.B. Riyadi, D. Setiadhi, A.D. Anggono, W.A. Siswanto, and H.H. Al-Kayiem, Analysis of mechanical and thermal stresses due to TiN coating of Fe substrate by physical vapor deposition, *Forces Mech.*, 4(2021), art. No. 100042.
[50] S.G. Ai, H.L. Fu, R.J. He, and Y.M. Pei, Multi-scale modeling of thermal expansion coefficients of C/C composites at high temperature, *Mater. Des.*, 82(2015), p. 181.
[51] J.J. Wang and F.Y. Ouyang, Nanotwinned medium entropy alloy CoCrFeNi thin films with ultra-high hardness: Modifying residual stress without scarifying hardness through tuning substrate bias, *Surf. Coat. Technol.*, 434(2022), art. No. 128191.
[52] Y.H. Lu and Y.G. Shen, Effect of carbon content on thermal stability of Ti–$C_x$–$N_y$ thin films, *J. Mater. Res.*, 23(2008), No. 3, p. 671.
[53] Y.X. Ou, H.Q. Wang, Q.S. Hua, B. Liao, and X.P. Ouyang, Tribocorrosion behaviors of superhard yet tough Ti–C–N ceramic

coatings, *Surf. Coat. Technol.*, 439(2022), art. No. 128448.
[54] R.Z. Li, S.H. Wang, J.B. Pu, *et al*., Study of NaCl-induced hot-corrosion behavior of TiN single-layer and TiN/Ti multilayer coatings at 500°C, *Corros. Sci.*, 192(2021), art. No. 109838.
[55] I. Dreiling, A. Haug, H. Holzschuh, and T. Chassé, Raman spectroscopy as a tool to study cubic Ti–C–N CVD coatings, *Surf. Coat. Technol.*, 204(2009), No. 6-7, p. 1008.
[56] L. Shan, Y.X. Wang, J.L. Li, *et al*., Tribological behaviours of PVD TiN and TiCN coatings in artificial seawater, *Surf. Coat. Technol.*, 226(2013), p. 40.
[57] K.L. Ming, Z.H. Zhang, and H.B. Li, *In situ* growth of $NaTiO_2$ nanotubes on $Ti_3C_2F_x$ for enhanced sodium ion batteries, *Mater. Lett.*, 309(2022), art. No. 131457.
[58] Y.X. Ou, H.Q. Wang, B. Liao, M.K. Lei, and X.P. Ouyang, Tribological behaviors in air and seawater of CrN/TiN superlattice coatings irradiated by high-intensity pulsed ion beam, *Ceram. Int.*, 45(2019), No. 18, p. 24405.
[59] B. Zhu, G.L. Kelly, and J. Mardel, An investigation of tribological properties of CN and TiCN coatings, *J. Mater. Eng. Perform.*, 13(2004), No. 4, p. 481.
[60] J.M. Lackner, W. Waldhauser, R. Ebner, *et al*., Room temperature pulsed laser deposited $(Ti,Al)C_xN_{1-x}$ coatings—Chemical, structural, mechanical and tribological properties, *Thin Solid Films*, 468(2004), No. 1-2, p. 125.
[61] J. Liu, S.J. Li, C. Wang, *et al*., Self-lubricating design strategy for thermally sprayed ceramic coatings by *in situ* synthesis of carbon spheres, *Surf. Coat. Technol.*, 446(2022), art. No. 128759.
[62] I. Çaha, A.C. Alves, C. Chirico, *et al*., Improved tribocorrosion behavior on bio-functionalized β-type titanium alloy by the pillar effect given by TiN reinforcements, *Surf. Coat. Technol.*, 415(2021), art. No. 127122.